Earth and Planetary Science Letters 457 (2017) 282–291

Contents lists available at ScienceDirect

Earth and Planetary Science Letters

www.elsevier.com/locate/epsl

Early aftershocks and afterslip surrounding the 2015 Mw 8.4 Illapel rupture

Hui Huang [a], Wenbin Xu [b,c], Lingsen Meng [a,*], Roland Bürgmann [b], Juan Carlos Baez [d]

[a] Earth Planetary and Space Sciences, University of California, Los Angeles, CA 90025, USA
[b] Berkeley Seismological Laboratory and Department of Earth and Planetary Science, University of California, Berkeley, CA 94720, USA
[c] Department of Land Surveying and Geoinformatics, The Hong Kong Polytechnic University, Kowloon, Hong Kong
[d] Centro Sismológico Nacional, Universidad de Chile, Santiago, Chile

ARTICLE INFO

Article history:
Received 10 July 2016
Received in revised form 28 September 2016
Accepted 30 September 2016
Available online 31 October 2016
Editor: P. Shearer

Keywords:
2015 Mw 8.4 Illapel earthquake
early aftershocks
repeating earthquakes
early afterslip

ABSTRACT

On 16 September 2015, the Mw 8.4 Illapel earthquake ruptured a section of the subduction thrust on the west coast of central Chile. The mainshock was followed by numerous aftershocks including some normal-faulting events near the trench. We apply a template matching approach to improve the completeness of early aftershocks within one month of the mainshock. To constrain the distribution of afterslip, we utilize repeating earthquakes among the aftershocks and perform a joint slip inversion of postseismic GPS and InSAR data. The results show that the aftershock zone abruptly expands to the south ~14 h after the mainshock while growing relatively continuously to the north within the first day. The repeating earthquakes accompanying the early expansion suggest that aseismic afterslip on the subduction thrust surrounding the coseismic rupture is an important triggering mechanism of aftershocks in addition to stress transfer or poroelastic effects. An energetic earthquake sequence near the trench initiated with a M 4.6 event ~3.5 h after the mainshock, suggesting delayed triggering by the static or dynamic stress changes induced by the mainshock. The spatial distribution of repeating earthquakes and the geodetic-inverted afterslip are consistent and appear to wrap around the large coseismic slip patch. Both data sets suggest that the largest cumulative afterslip is located at ~30.5°S to the north of the mainshock rupture zone. The estimated postseismic moment released in the first ~24 days of afterslip is equivalent to an earthquake of Mw 7.5. The afterslip illuminates the velocity strengthening sections of the plate interface that surround the mainshock rupture, consistent with plate coupling models inferred from interseismic GPS velocities.

1. Introduction

The west coast of central Chile is characterized by the slightly oblique subduction of the Nazca plate underneath the South American plate, at a rate of ~68 mm/yr (Fig. 1a, Angermann et al., 1999; Métois et al., 2012). On 16 September 2015, the Mw 8.4 Illapel earthquake nucleated at 31.553°S, 71.864°W at a depth of 11.1 km, ~30 km offshore, according to the catalog determined by the Centro Sismológico Nacional (CSN; http://www.sismologia.cl). There are two major oceanic structures of the subducting Nazca plate around the 2015 Illapel event: the Challenger Fracture Zone (CFZ) and the Juan-Fernández Ridge (JFR). The JFR intersects the trench at ~32.5°S but the exact intersection of the CFZ with the trench remains unclear and high resolution multi-beam bathymetry data do not clearly image the continuation of the fracture zone to the trench (Fig. 1a, Lange et al., 2016; Yáñez et al., 2001). The CFZ is associated with a crustal age offset of 3.5 Myr while the JFR represents a hot spot chain. Several large historical earthquakes occurred around the 2015 Illapel rupture zone, including the 1906 M 8.4 earthquake to the south and the 1922 M 8.4 earthquake to the north (Fig. 1a). Finite slip models and back-projection analyses of the Illapel event suggest that the rupture mainly extends to the north of the hypocenter (e.g., Heidarzadeh et al., 2016; Melgar et al., 2016; Okuwaki et al., 2016; Tilmann et al., 2016). The seismic energy release of the earthquake was frequency dependent with a lower frequency section, corresponding to the area of greatest moment release, updip of a zone of strong high-frequency radiation (Melgar et al., 2016; Yin et al., 2016).

The early aftershocks carry key information for understanding the mechanism of aftershock triggering processes, including the

* Corresponding author.
E-mail address: meng@ess.ucla.edu (L. Meng).

http://dx.doi.org/10.1016/j.epsl.2016.09.055
0012-821X/

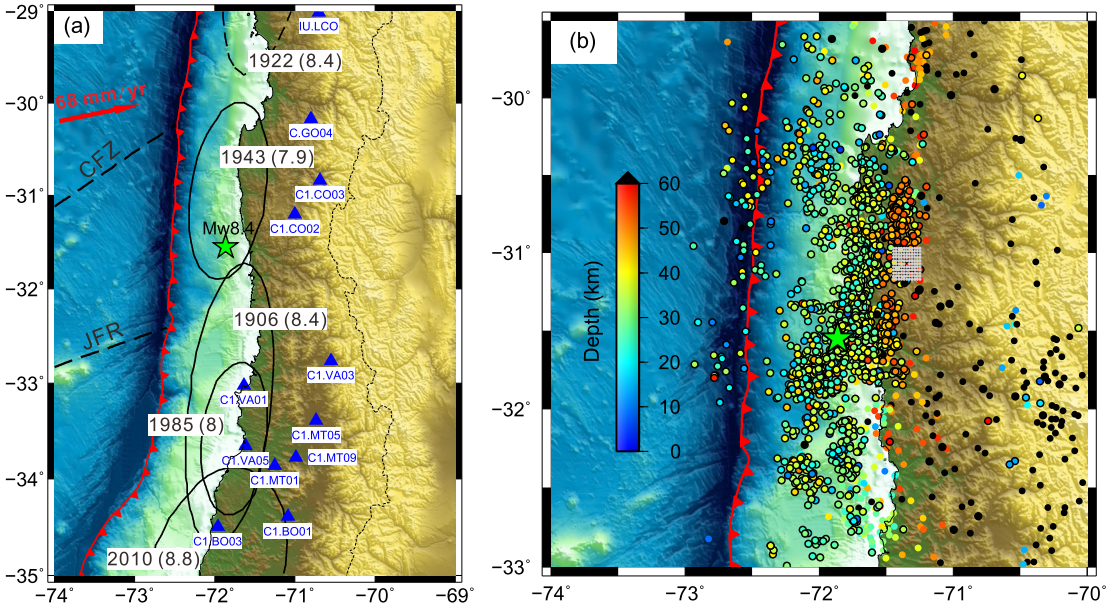

Fig. 1. (a) Map showing the 12 stations (blue triangles) used for matched-filter detection in this study. The black and dashed ellipses denote maximal rupture zones of instrumental and historical megathrust earthquakes (Métois et al., 2012). The green star denotes the epicenter of the 2015 Illapel M 8.4 mainshock. The two dashed lines indicate the Challenger fracture zone (CFZ) and Juan-Fernández Ridge (JFR). (b) The solid colored circles show the template locations color-coded by depth, with black dots denoting events with depth >60 km. The catalog is acquired from the Centro Sismológico Nacional, Universidad de Chile (CSN). The circles with outlines denote the aftershocks until 27 October 2015 while others denote events occurring from 1 January 2015 to the mainshock. The rectangular array of gray dots surrounding the template show an example of candidate grid locations used in matched-filter detection. (For interpretation of the references to color in this figure legend, the reader is referred to the web version of this article.)

role of aseismic afterslip (e.g., Meng et al., 2015; Peng and Zhao, 2009). According to the CSN catalog, the majority of early aftershocks occurred around the mainshock rupture with few events near the trench (Fig. 1b). However, due to the contamination by the mainshock coda and overlapping multiple phases, a large portion of early aftershocks may be undocumented in routine catalogs (Peng and Zhao, 2009). The matched-filter method is effective and widely used to recover uncataloged events before or after large earthquakes, which have been used to reveal the important role of aseismic slip in foreshock migration (e.g., Kato et al., 2012) and aftershock expansion (e.g., Lengliné et al., 2012) associated with the 2011 Tohoku earthquake.

Aseismic slip is an important fault behavior on plate boundary faults that contributes to the release of accumulated strain (e.g., Igarashi et al., 2003; Ozawa et al., 2011). The kinematics of secular aseismic slip on the plate interface can be effectively modeled by inversion of interseismic GPS velocities. Fault areas with high coupling are locked over the interseismic period while areas with weak coupling are partially releasing stress by aseismic sliding via steady fault creep, spontaneous slow slip events and postseismic afterslip. Métois et al. (2014) find that the plate coupling around the 2015 Illapel epicentral area (31°S–33°S) is very high (nearly 100%), whereas Tilmann et al. (2016) infer that the plate boundary slip deficit is relatively low between 31°S–32°S.

An alternative method to measure the in-situ aseismic slip is by repeating earthquakes (e.g., Igarashi et al., 2003; Kato et al., 2012; Uchida and Matsuzawa, 2013). Repeating earthquakes are commonly interpreted as recurrent ruptures of asperities driven by surrounding aseismic slip (Nadeau and Johnson, 1998; Nadeau and McEvilly, 1999). While it can be challenging for geodetic postseismic models to separate the contributions from different postseismic relaxation processes (i.e., afterslip, viscoelastic relaxation and poroelastic rebound), in the portions of the megathrust where small asperities are available the repeating earthquakes directly image the spatial distribution and magnitude of aseismic afterslip (e.g., Uchida et al., 2004; Meng et al., 2015). On the other hand, geodetic measurements can constrain the aseismic slip where repeating earthquakes do not exist. Joint analysis of geodetic measurements and repeating earthquakes allows for much improved characterization of postseismic deformation and the determination of the contributing deformation processes (e.g., Shirzaei et al., 2013).

In this study, we investigate the spatio-temporal pattern of early aftershocks and afterslip of the 2015 Mw 8.4 Illapel earthquake. We perform template matching to obtain a more complete record of the aftershock sequence in the first month, which is further used to find repeating earthquakes that illuminate the area of slow slip following the mainshock. We also use postseismic GPS and InSAR data to constrain the distribution of early afterslip following the mainshock. Finally we discuss the spatio-temporal pattern of the aftershock sequence and afterslip in comparison to the coseismic slip models and interseismic coupling models. The results shed light on the important role of aseismic slip in the early expansion of the aftershock zone and the release of stress on the partially coupled plate interface.

2. Matched-filter detection and repeating earthquake analysis

We first improve the early aftershock catalog by the matched-filter method (e.g., Peng and Zhao, 2009; Zhang and Wen, 2015). We collect three-component broadband velocity seismograms (40-Hz sampling rate) at 12 stations (Fig. 1a) within 3 degrees from the mainshock epicenter (31.553°S, 71.864°W). We acquire continuous seismograms spanning from 16 September 2015 to 16 October 2015 from the Incorporated Research Institutions for Seismology (IRIS) Data Management Center (DMC). Most of the stations recorded data continuously during the study period (Fig. S1). The template catalog (1973 events, from 1 January 2015 to 27 October 2015, Fig. 1b and Table S1) is obtained from the CSN website (http://www.sismologia.cl). The template waveforms are windowed from 2 sec before to 6 sec after the theoretical S arrival time. The travel times are calculated based on a 1D velocity model used by the CSN for event location in the study region (Ruiz et al., 2016).

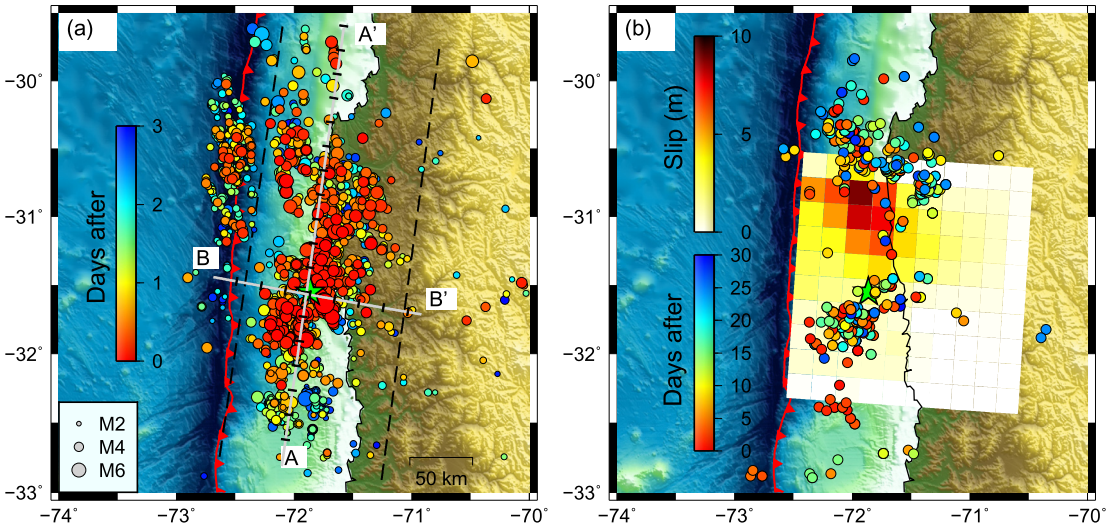

Fig. 2. (a) Map view of the combined dataset of newly detected events and the CSN catalog for first 3 days after the mainshock. The color denotes the differential origin time after the mainshock while the size scales with magnitude. The tick spacing on profiles AA' and BB' is 20 km. The black dashed lines indicate the western and eastern limits for seismicity used in along-strike projections (Figs. 3a and 3b). (b) Comparison of repeater activity within one month after the mainshock with the co-seismic model from An and Meng (2016).

Both template and continuous waveforms are band-passed between 1 and 6 Hz with a fourth-order Butterworth filter. For a template to be analyzed, a minimum of 12 channels and a signal-to-noise ratio (SNR) greater than 5 are required. The SNR is estimated by comparing the template waveforms to a 8 sec time window ending 4 sec before the theoretical P arrival time. We compute the cross-correlation coefficient (CC) between the template waveforms and the corresponding continuous waveforms in a moving window with an increment of 0.025 s. The CC trace as a function of time is then averaged over all available channels. To better align the noncoherent CC traces induced by spatial separation of real events from the template, we shift the CC traces according to the theoretical S travel time difference between the grid location and the centered template before stacking (Zhang and Wen, 2015). Due to the poor depth sensitivity of S wave travel times, we only search the horizontal plane centered at each template with a grid of 0.2° by 0.2° and a spacing of 0.02° along both the latitude and longitude directions (Fig. 1b). The whole template dataset and their associated search grids cover a wide area around the mainshock, thus providing an excellent estimate of the locations of detected events. The detection threshold is set at 11 times the median absolute deviation (MAD) of each daylong CC trace (e.g. Fig. S2), comparable to previous studies (e.g., Peng and Zhao, 2009; Kato et al., 2012). To remove duplicate detections, if the same segment of continuous records (over 4 sec of overlap) is associated with multiple detections, only the template with highest mean CC is kept. Then the magnitude of each detected event is estimated according to the median value of the maximum amplitude ratios in all channels, assuming that one magnitude unit increase relative to the local magnitude in the template catalog corresponds to a tenfold amplitude increase (Peng and Zhao, 2009). A total of 7571 new events (including 7558 aftershocks) are detected from 16 September 2015 to 16 October 2015, ∼5.4 times the number of events in the CSN catalog (1398 events) in the same time period.

Next we extract the repeating earthquakes from the new combined catalog (M >= 2.5, from 1 January 2012 to 23 November 2015, Table S1). The analysis procedure is similar to previous studies (e.g., Igarashi et al., 2003; Uchida and Matsuzawa, 2013; Meng et al., 2015) and briefly described here. We convert the local magnitude (Ml) to moment magnitude (Mw) by using the same Ml–Mw relations as Meng et al. (2015). We only consider event pairs with hypocentral separations of less than 30 km and focal depths shallower than 80 km. The seismograms at 21 stations (Fig. S3) are acquired from the IRIS DMC. The vertical seismograms are bandpass filtered according to the source size: 1–4 Hz for event pairs with Mw >= 3 or 1–8 Hz otherwise (Igarashi et al., 2003; Meng et al., 2015). Waveforms are initially windowed from 3 s before the theoretical P-wave arrival times to 15 s after the S-wave arrival to include enough S wave energy. If the CC exceeds 0.95 and the magnitude difference estimated from the logarithm of the maximum amplitude ratio is smaller than 0.5 at two or more stations, the two events are classified as belonging to a group of repeating earthquakes (e.g., Fig. S4). Then all groups with common events are linked into the same repeater sequence.

A total of 291 sequences (712 events) of repeating earthquakes are identified. A large portion (∼87%) of repeating earthquakes occur after the mainshock. There are 77 sequences that occur within a period of less than 7 days. Such isolated short-term sequences have been categorized as burst-type repeaters in previous studies (Igarashi et al., 2003; Templeton et al., 2008). They may occur on fault planes within the overriding or the subducting plate and don't reflect creep on the plate boundary thrust (Igarashi et al., 2003).

3. Spatio-temporal evolution of early aftershocks

Fig. 2a shows a map view of the first three days of aftershocks, color-coded by the occurrence time since the mainshock. It shows that the early aftershocks migrate both northward and southward with time (symbol colors changing from red to blue). The triggered events close to the trench are mostly located at the northern side of the mainshock rupture. The repeating earthquakes found among the aftershocks in the first month are mainly distributed to the north, south and downdip of the large coseismic slip zone (Fig. 2b). Some repeaters are also identified among the near-trench events. Fig. 3 shows the spatio-temporal evolution of early aftershocks and repeating earthquakes projected onto the along-strike profile AA' and along-dip profile BB' (Fig. 2a). In the along-strike direction, to exclude events near the trench, only the aftershocks between the dashed lines in Fig. 2a are plotted. The along-strike aftershock expansion is mainly seen within the first day after the mainshock. To the south of the rupture zone, the aftershocks within the first ∼12 h contain several M >= 6 events and repeaters and are confined within ∼60 km distance from the mainshock epicenter. At

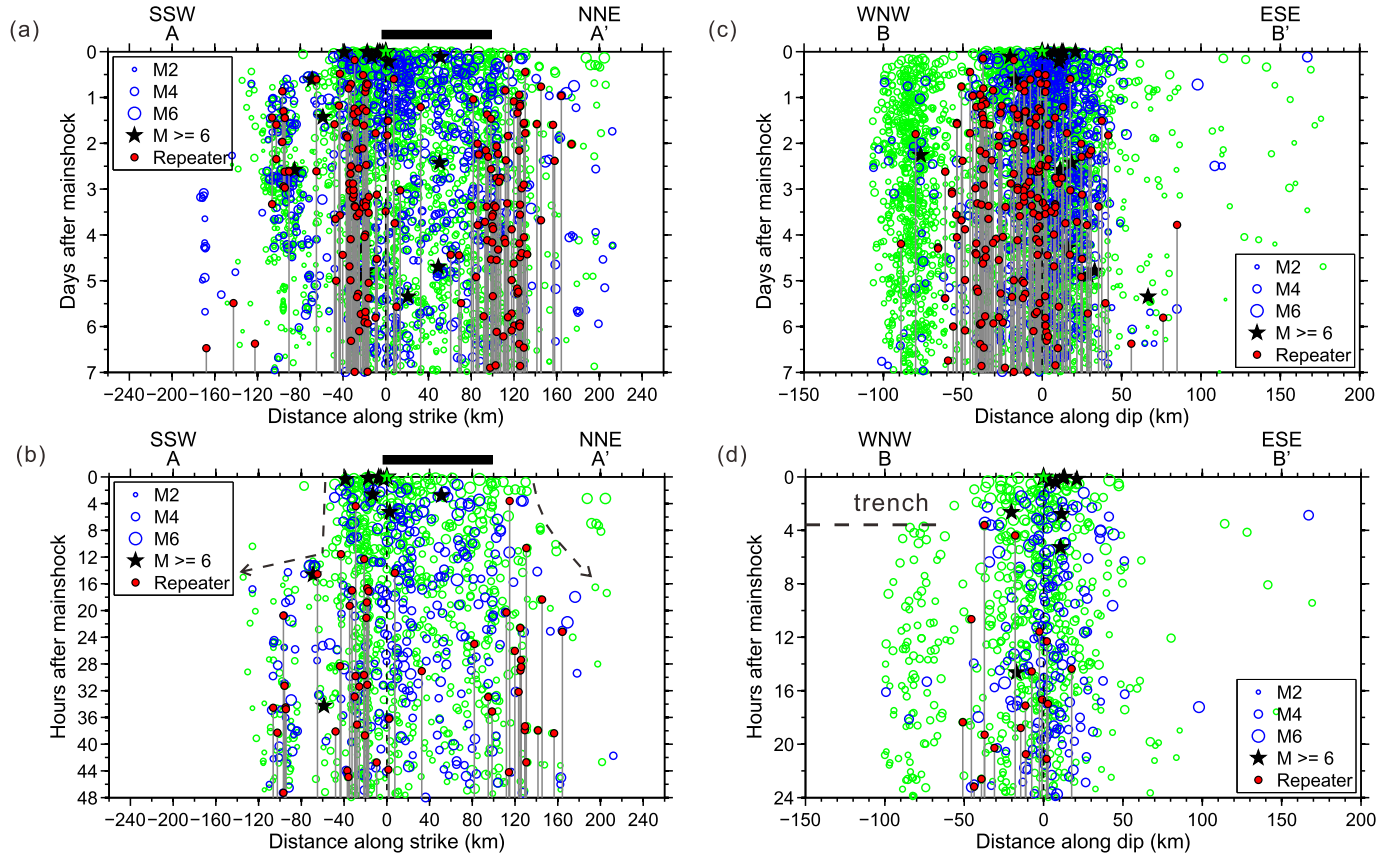

Fig. 3. Migration of very early aftershocks within 7 days (a and c), 2 days (b) and 1 day after the mainshock (d). (a) and (b) show the along-strike distance of seismicity from between the black dashed lines (Fig. 2a) projected onto AA' with the mainshock epicenter at zero. The gray lines connect each repeating earthquake sequence, which are plotted at the average location. The two dashed lines depict the migratory patterns of aftershocks within the first day. (c) and (d) show the along-dip distance projected onto BB'. See Fig. 2 for the profile locations. The black bars on top of (a) and (b) show the extent of coseismic slip (larger than 20 percent of the maximum slip value of An and Meng, 2016's model).

~14 h after the mainshock there was a significant southward expansion to ~130 km, in contrast to the more steady southern aftershock expansion observed by Lange et al. (2016). In contrast to the south the northward expansion in the first day appears more continuous (from ~140 km to ~210 km) with no M >= 6 events and fewer repeaters (Figs. 3a and 3b). The along-dip expansion is not clear within the first day after the mainshock (Figs. 3c and 3d). It is notable that the majority of repeating earthquakes wrap around the zone of large coseismic slip (Figs. 2b and 3a), in contrast to relatively more spatial overlap of the first 30-day aftershocks with the coseismic slip zone (Fig. S5). The area outside of the main coseismic slip zone includes many repeating groups recurring at short time intervals (connected with red lines), suggesting fast afterslip there.

A lot of new events (M ~0.9–4.6) are detected near the trench in an elongated zone extending from ~31°S to 30°S (Figs. 2a, 3c and 3d). This earthquake sequence near the trench initiated with a M 4.6 event (30.52°S, 72.45°W, blue star in Fig. 4a), which is detected by the M 5 template with normal faulting mechanism reported by NEIC (Fig. 4a). Some other events also have normal faulting mechanisms as reported by NEIC or GEOFON, with the strike direction nearly parallel with the Chilean trench axis (Fig. 4a). It is notable that the whole sequence started ~3.5 h after the mainshock (Fig. 3d). The apparent time delay persists when lowering the detection threshold to 10 times the MAD or tightening to 15 times the MAD (Fig. S6), indicating a delayed response to the stress change induced by the mainshock in this area. Among these events, there are 10 repeaters (5 doublets, Figs. 4a and 4b). Two doublets have recurrence times smaller than 3 days while the other three doublets recur within 7–20 days, suggesting there may have been some triggered short-term fault creep in that area. In the first several hours, the seismicity appears to migrate northward along the trench axis from the location of the first M 4.6 event (Figs. 4b and 4c). This migratory pattern can still be observed when the threshold is increased to 15 times the MAD (Fig. S7).

4. Early afterslip model from repeating earthquakes, GPS and InSAR data

We first estimate the early postseismic slip on the subduction thrust from the repeating earthquake data. We exclude burst-type repeater sequences spanning time intervals of less than 7 days, which may not reflect creep on the plate boundary (Templeton et al., 2008). We use the empirical relation introduced by Nadeau and Johnson (1998) to convert the seismic moment of repeating earthquakes into an estimate of corresponding aseismic-slip increments on the surrounding fault. We apply this aseismic slip estimate to patches of varying sizes around the repeater sequences. Assuming a crustal shear modulus of 30 GPa, the aseismic moment release estimated from the repeaters is in the range of Mw 7.16–7.51, depending on the prescribed patch size (Fig. 5). Note that the total amount of seismic moment of repeaters within the same period is 7.07e+17 N m (Mw 5.83), significantly smaller than the estimated aseismic moment. Because the repeaters are only capable of estimating aseismic slip at positions where small asperities are available, this estimate may not fully illuminate the spatial extent of afterslip. Fig. 6 shows the different time series of repeater-inferred afterslip in the northern, southern and downdip parts of

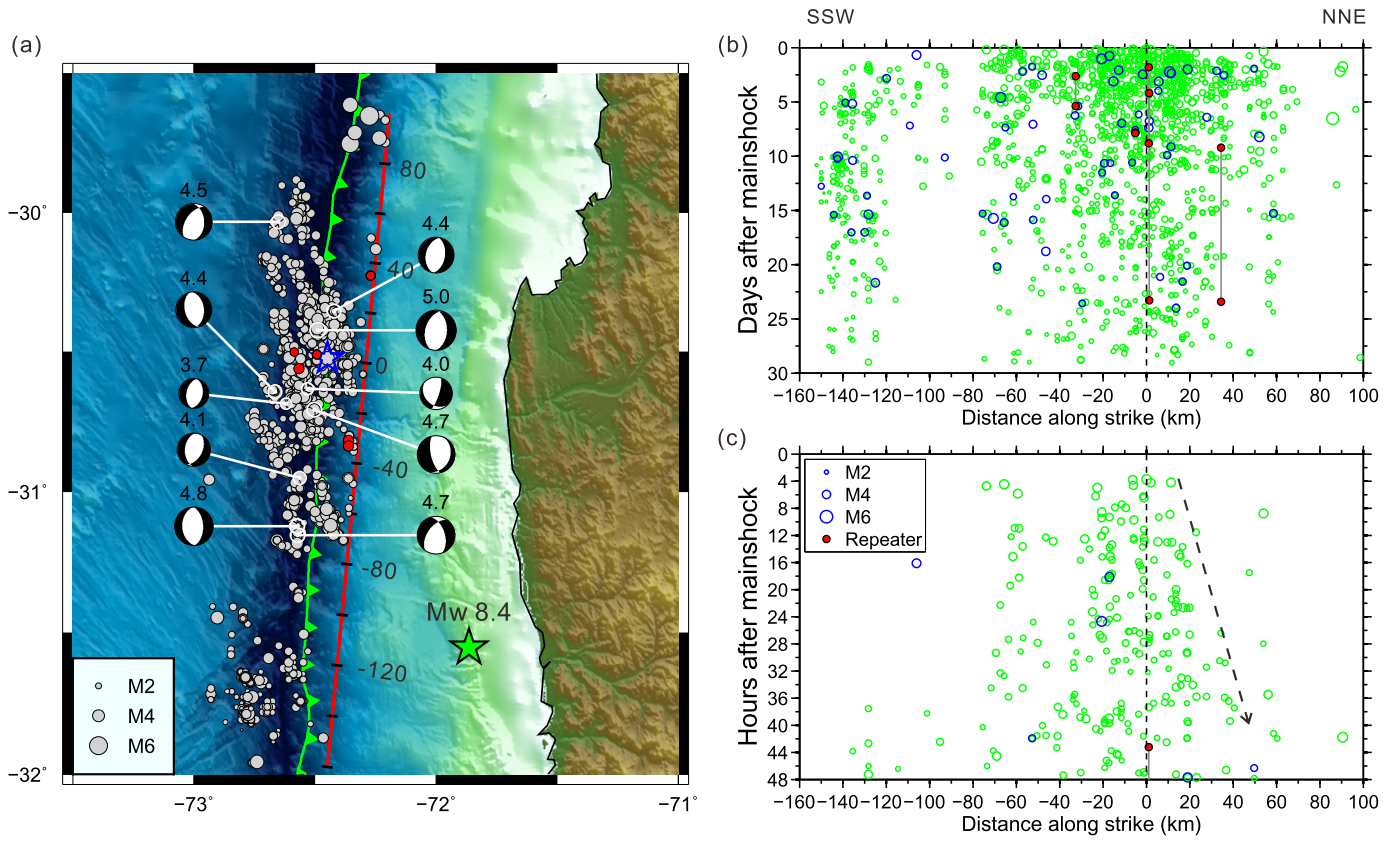

Fig. 4. (a) Events near the trench (to the west of the red line) within one month after the Mw 8.4 mainshock. The red dots denote the 10 repeaters during this time period. The available focal mechanisms of some events posted at NEIC or GEOFON are shown. The red line indicates the profile (marked distances in km) where events are projected in (b) and (c), which show the spatio-temporal pattern of aftershocks and repeaters within the first 30 days and 2 days after the Mw 8.4 mainshock, respectively. Note that the first event of the whole sequence is a M 4.6 event with projected distance 0 km, shown as a blue star in (a). The dashed line in (c) depicts the possible northward migration in the first several hours. (For interpretation of the references to color in this figure legend, the reader is referred to the web version of this article.)

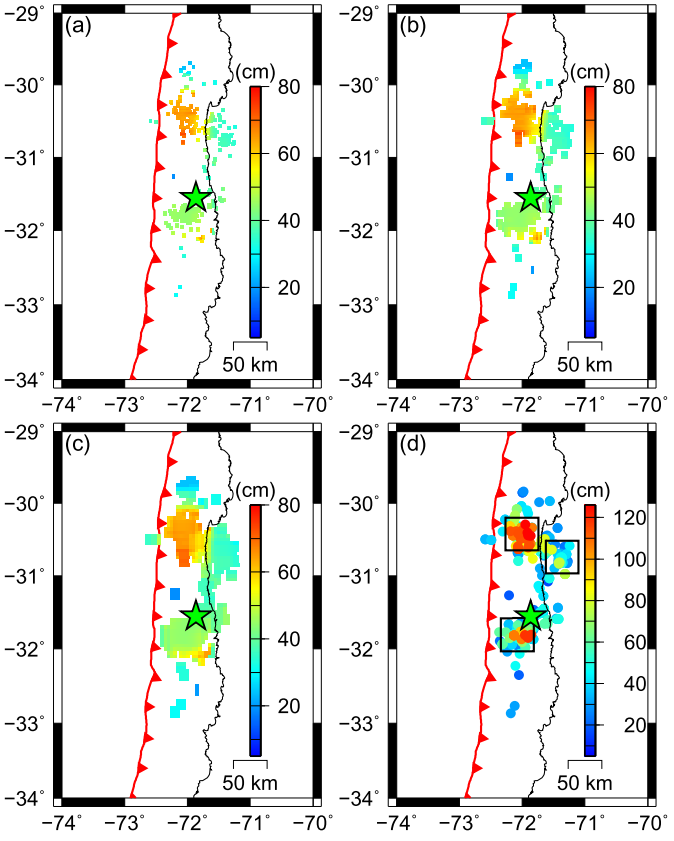

Fig. 5. Estimated afterslip distribution from repeating earthquakes during the first month after the mainshock in (a) 0.05° × 0.05° bins (moment 6.94e+19 N m, Mw 7.16), (b) 0.1° × 0.1° bins (1.57e+20 N m, Mw 7.40) and (c) 0.15° × 0.15° bins (2.34e+20 N m, Mw 7.51). The afterslip value is averaged over a 0.5° × 0.5° grid centered at each moving window. (d) shows the individual repeating earthquakes colored by the cumulative slip during one month after the mainshock. The three boxes (50 km × 50 km) in (d) show the northern, southern and downdip regions from estimating afterslip time series in Fig. 6. Only the repeater sequences that span a time interval of over 7 days are used.

the mainshock rupture area (Fig. 5d). Generally the afterslip rate is highest immediately after the mainshock, followed by a decrease with time. The northern patch accumulates the largest afterslip compared to the southern and downdip patches. The inferred afterslip rate fluctuates during the study period, which could reflect the non-steady expansion of the afterslip zone and accelerations associated with large aftershocks. The afterslip series in the northern and southern patch can be well fitted by the afterslip model (Fig. S8, Marone, 1998).

We further perform an afterslip inversion from both GPS and InSAR observations. The GPS time series of motions with respect to stable South America are from continuously operating stations in the region processed with the Bernese GPS processing software at the CSN (Ruiz et al., 2016). The post-seismic GPS time series in the east, north, and vertical directions for four selected stations are shown in Fig. 7. Significant westward to west-northwestward post-seismic displacements of ∼150 mm are observed at station PRFJ during the first 70 days after the main-shock. The eastward displacements can be well fitted with a logarithmic function. This function can also fit the northward motion at which the stations are located closer to the epicenter. The linear function, however,

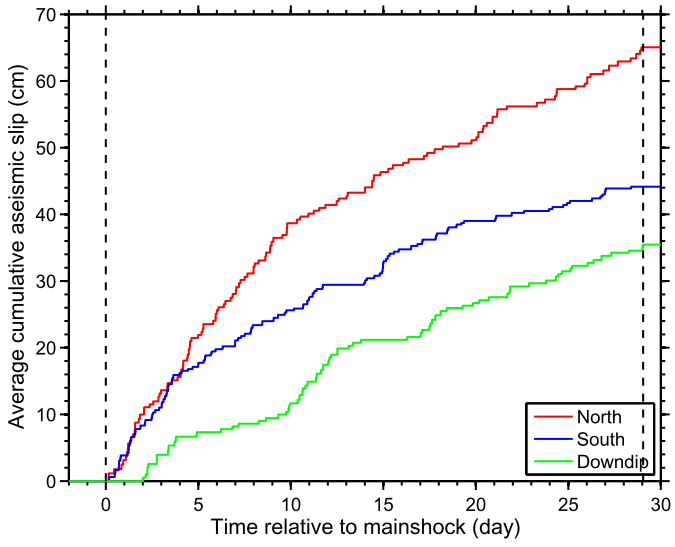

Fig. 6. The average cumulative aseismic slip inferred from the repeaters within the northern patch (red curve) and the southern patch (blue curve) and downdip patch (green curve). The curves are averaged between different repeater sequences within the three boxes in Fig. 5d. The two dashed vertical lines mark the period when the catalog is improved by matched-filter analysis. (For interpretation of the references to color in this figure legend, the reader is referred to the web version of this article.)

seems to fit the data better in some components (Fig. 7), which needs to be further checked with longer data. The Sentinel-1A SAR data are in the Terrain Observation by Progressive Scans (TOPS) mode (Salvi et al., 2012). In this mode, the antenna sweeping in the azimuth direction can cause strong Doppler centroid variation introducing steep azimuth phase ramps across the interferogram. To remove these phase discontinuities, the spectral diversity method is used after applying the intensity cross correlation between the master and slave images. We process the data with the GAMMA software and use the Shuttle Radar Topography Mission (SRTM) 3 arc/second DEM (Farr et al., 2007) to simulate and eliminate the contribution of topography to the measured phase changes. We multilook and filter the interferograms to mitigate noise (Goldstein and Werner, 1998). Finally, we unwrap the interferograms using the minimum cost flow (MCF) method (Chen and Zebker, 2000) and geocode them into the WGS84 coordinate system. We generate two interferograms from three Sentinel-1A SAR images collected along the descending orbit (Figs. 8a and 8b) and two interferograms from three ascending-orbit acquisitions (Figs. 8c and 8d). Figs. 8a and 8c show postseismic ground deformation for a period of 24 days starting from one day (descending) and three days (ascending) after the mainshock, respectively, Figs. 8b and 8d show postseismic ground deformation spanning 48 days. The interferograms from the descending orbit have less noise, possibly because they were acquired in the early morning, while the ascending orbit acquisitions were obtained in the late afternoon leading to more atmospheric noise. The earlier interferogram

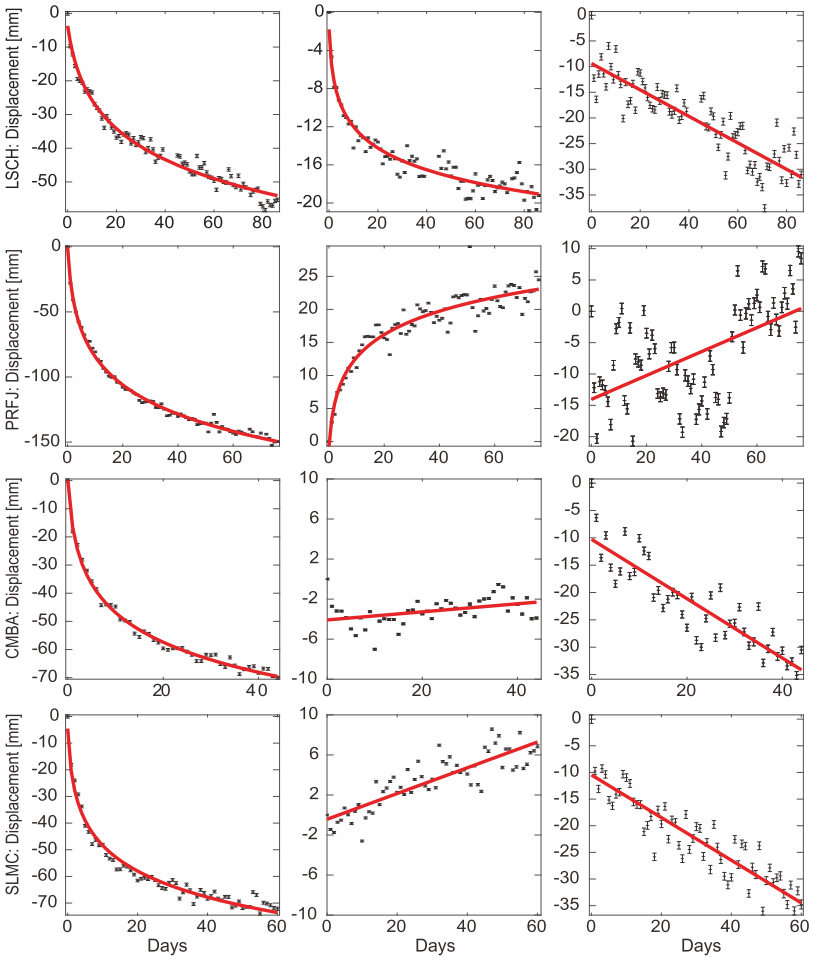

Fig. 7. Post-seismic GPS time series at station LSCH (top row), PRFJ (second row), CMBA (third row) and SLMC (bottom row). The scattered points show the temporal variations found in the east component (first column), north component (second column) and vertical component (third column). The thick solid red lines show the least-squares fit with a logarithmic or linear function. (For interpretation of the references to color in this figure legend, the reader is referred to the web version of this article.)

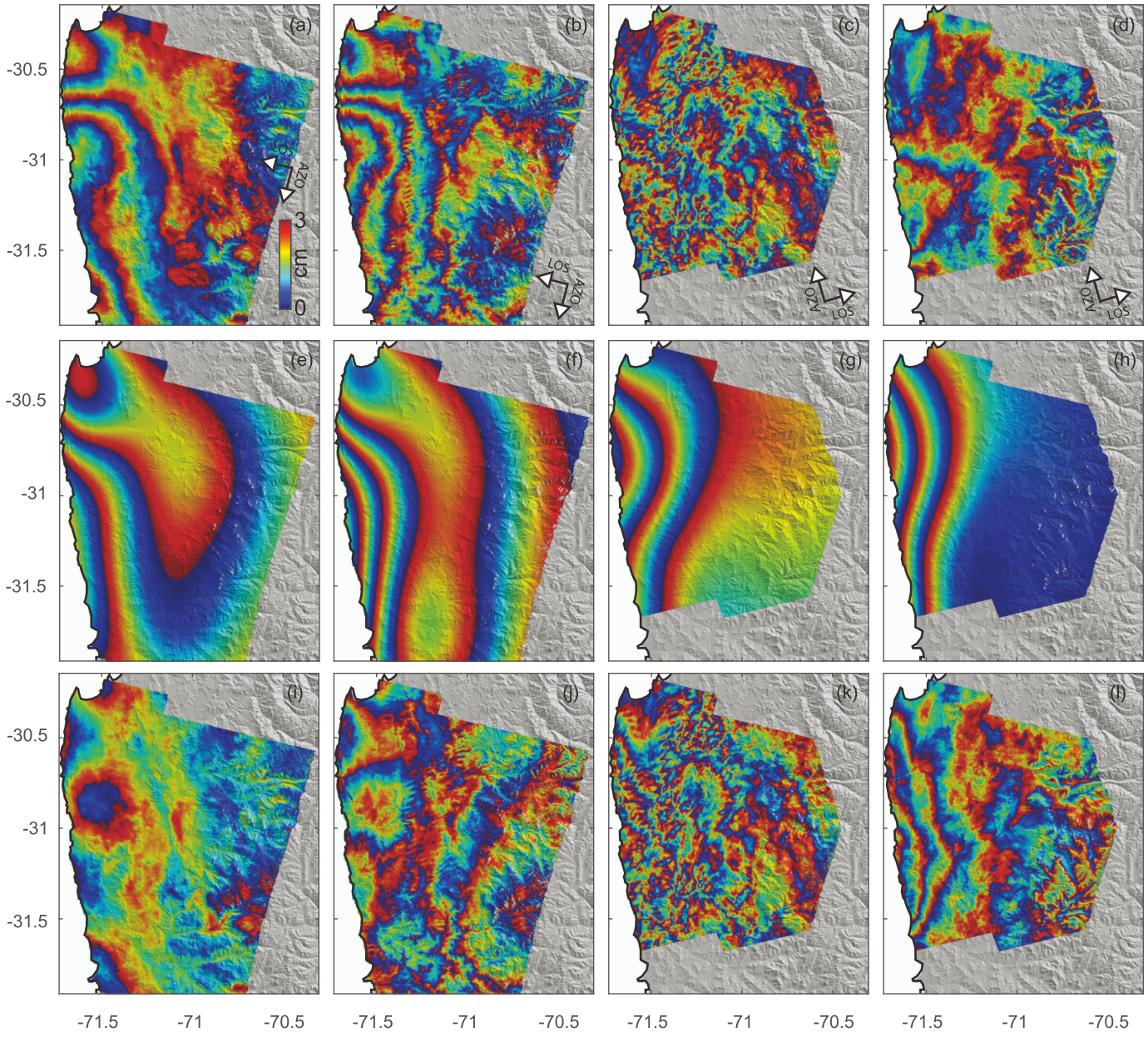

Fig. 8. Postseismic InSAR data and line-of-sight displacements from modeled afterslip. One fringe corresponds to 3 cm of line-of-sight (LOS) displacement. (a–b) Observed interferograms from the descending orbit spanning 17 Sep. and 11 Oct. and 17 Sep. and 4 Nov., respectively. (c–d) Observed interferograms from the ascending orbit spanning 19 Sep. and 13 Oct. and 19 Sep. and 6 Nov., respectively. (e–h) model predictions of (a–d), (i–l) residuals.

(Fig. 8a) shows ∼2 fringes of surface displacement from September 17 to October 11 (i.e., ∼6 cm in the radar line-of sight (LOS)) near the coastline at 31°S, while the interferogram from September 17 to November 4 (Fig. 8b) shows ∼4 fringes (∼12 cm in LOS). The interferograms from the ascending orbit are contaminated by atmospheric effects, but the 48-day interferogram (Fig. 8d) shows ∼2 fringes of apparent surface displacement (i.e., ∼6 cm in LOS).

We jointly invert the postseismic GPS data from 17 GPS stations and the unwrapped interferograms from both ascending and descending orbits using a triangular dislocation model in a homogeneous, isotropic, elastic half-space (Nikkhoo and Walter, 2015) with Poisson's ratio and shear modulus of 0.25 and 30 GPa, respectively. We adapt the fault geometry from SLAB 1.0 (Hayes et al., 2012), which is publicly available from the USGS website (http://earthquake.usgs.gov/data/slab/). In the inversion, we only invert for the fault thrust slip by fixing the rake angle to be 90°. To prevent oscillatory solutions, the inversion is regularized with positivity and smoothness constraints. In general, slip increases with time and the slip pattern is spatially stable over time (Fig. 9). The position of the postseismic slip maximum is located north of peak coseismic slip. In the first ∼24 days after the mainshock, the maximum slip magnitude is 53 cm (Fig. 9a), and the moment release is 2.3×10^{20} N m corresponding to Mw 7.5. The rms misfit is 1.6 cm. In comparison, during the first ∼50 days after the mainshock, the maximum slip increases to 60 cm north of the epicenter, and a zone of less slip of 45 cm is located south of the epicenter (Fig. 9b). The 50-day moment release is 2.76×10^{20} N m corresponding to Mw 7.56. The rms misfit is 1.7 cm. The location of afterslip from the geodetic inversion is generally consistent with the location of repeaters (Fig. S9). The cumulative afterslip from the geodetic inversion is generally close to or smaller than the repeater-inferred cumulative afterslip, with the largest difference observed to the south of the mainshock (Fig. S9). This may be due to data uncertainties, smoothing in the geodetic inversion, assumptions regard-

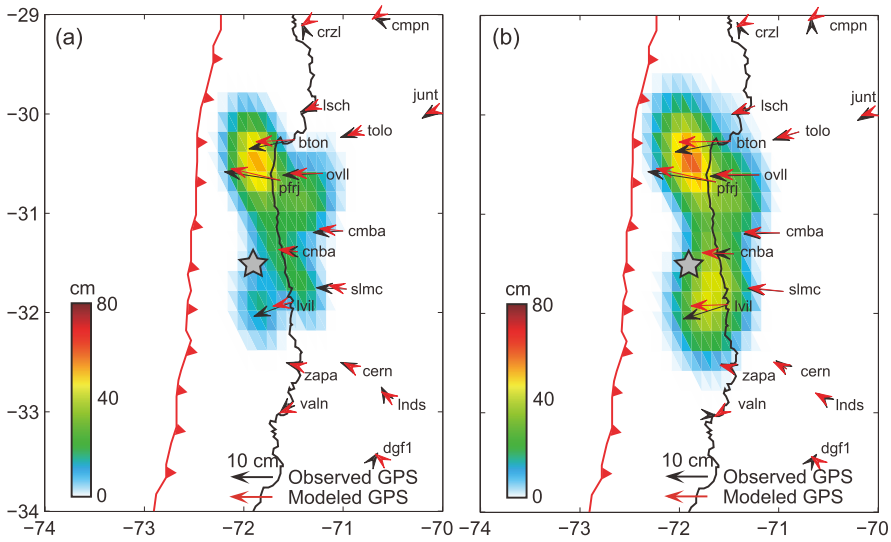

Fig. 9. Afterslip distribution estimated from the joint inversion of InSAR and GPS data (a) between 17 September and 13 October and (b) 17 September and 6 November, respectively. Black and red arrows show observed and modeled GPS horizontal displacements. (For interpretation of the references to color in this figure legend, the reader is referred to the web version of this article.)

ing elastic earth structure and fault geometry or the uncertainty of the empirical relation used to convert repeater moments to aseismic slip. Both the seismic and geodetic data sets show that there are two predominant patches of afterslip to the north and south of the mainshock rupture (Fig. 9). The northern patch at ∼30.5°S is characterized by larger cumulative aseismic slip than the southern patch during the first month (Figs. 5 and 9a). The afterslip also extends downdip of the coseismic rupture zone (Fig. 9).

5. Discussion and conclusions

5.1. The spatio-temporal evolution of early aftershock sequence

In our study, the observed along-strike expansion of early aftershocks within the first day raises the question of aftershock triggering mechanisms. Both static and dynamic triggering may play an important role in the aftershock zone surrounding the mainshock rupture (Felzer and Brodsky, 2006; Gomberg et al., 2003; van der Elst and Brodsky, 2010). In addition, aseismic afterslip was found to be the driving mechanism of aftershock zone expansion of other events (e.g., Perfettini and Avouac, 2004; Hsu et al., 2006), including the 2004 Mw 6.0 Parkfield earthquake (Peng and Zhao, 2009) and the 2011 Mw 9.0 Tohoku-Oki earthquake (Lengliné et al., 2012). For the 2015 Illapel earthquake, Tilmann et al. (2016) found that most of the thrust-faulting aftershocks are distributed in areas of positive Coulomb stress change, suggesting the importance of static triggering and/or triggering by afterslip driven by the stress increase. Lange et al. (2016) found faster along-strike migration of aftershocks to the south (5 km/day) than to the north (2.5 km/day) within the first day. Our results show that the aftershocks accompanied by repeaters suddenly advanced to the south at ∼14 h after the mainshock while they steadily migrated to the north. Repeating earthquakes, indicative of recurrent ruptures of the same fault patch, are primarily induced by surrounding aseismic slip (Nadeau and Johnson, 1998). In our study, the colocation of repeaters and afterslip inverted from independent geodetic data supports the viewpoint that repeaters are mainly driven by afterslip on the megathrust. The sudden southward expansion may be explained by propagating afterslip encountering a relatively strong asperity, which finally breaks ∼14 h later in an Mw 6.0 event due to the continuous loading by afterslip. A similar sudden expansion is observed in the aftershock zone of the 2004 Mw 6.0 Parkfield earthquake migrating towards the locked portion of the San Andreas fault (Peng and Zhao, 2009) and the aftershock zone of the 2007 Mw 6.7 Noto-Hanto earthquake when encountering a complex segmented fault zone (Kato and Obara, 2014). In contrast, the relatively continuous northward expansion within the first day may be related to the wide distribution of areas with velocity-strengthening fault properties to the north (will be discussed in section 5.2). This suggests the spatial heterogeneity of fault frictional properties on the fault and/or complex structures such as subducted seamounts to the south of the Illapel rupture (e.g., Laursen and Normark, 2002; Yáñez et al., 2001) may control the pattern of aftershock expansion. Overall, our results suggest that stress-driven afterslip is an important mechanism for the triggering and early expansion of aftershocks of the Illapel event in addition to other possible physical processes, such as stress transfer or poroelastic effects.

In addition, the observation of a large cluster of triggered events near the trench, which initiated with a delay of ∼3.5 h, is intriguing. They may occur within the oceanic plate, on the shallow plate interface and/or within the hanging wall of the megathrust. Some of these events are normal-faulting earthquakes, consistent with increased tension in the outer rise (Tilmann et al., 2016). A large number of triggered outer-rise events is often seen as an indicator of large coseismic slip near the trench (Christensen and Ruff, 1983; Lay et al., 2009). This is consistent with significant slip reaching the trench revealed by the back-projection and finite-fault inversion studies of the Illapel earthquake (e.g., Melgar et al., 2016; Tilmann et al., 2016). The delayed initiation of the sequence may indicate that the immediate static stress at the outer rise was not sufficient to instantly trigger events and that an aseismic process, such as slow slip or fluid flow, was needed to initiate this sequence. This short delay time may also indicate time-dependent earthquake nucleation processes (e.g., Dieterich, 1994). Another possible effect is dynamic triggering, which is often observed in triggering events at remote distances by passing surface waves (e.g., Hill et al., 1993) but also can promote earthquakes nearby a rupture (e.g., Kilb et al., 2000). A delayed dynamic triggering response may reflect nonlinear frictional fault properties, fluid migration, and/or aseismic fault slip (Hill and Prejean, 2015). Our results suggest that the events near the trench migrate along the trench axis in the first several hours. This might suggest the existence of aseismic slip and/or fluid flow to cause the delayed triggering and migration of events. Slow slip may be indicated by

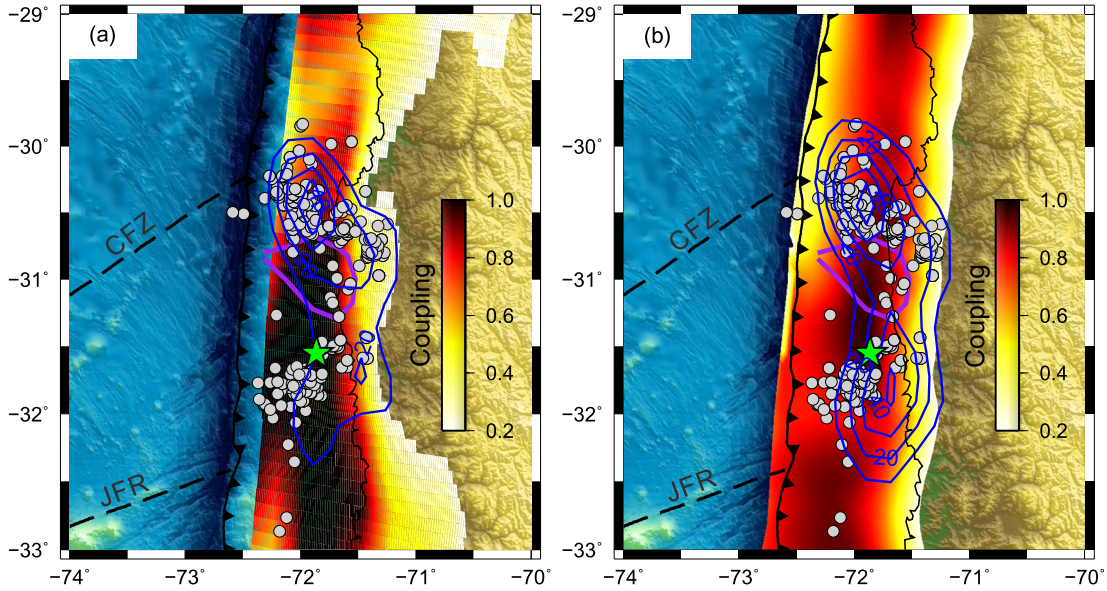

Fig. 10. First one-month repeating earthquake distributions (gray circles) and afterslip (blue contours in cm) from geodetic inversion between (a) 17 September and 13 October and (b) 17 September and 6 November. The plate coupling model in (a) is from Métois et al. (2014), which uses GPS data from 2004 to 2012; the model in (b) is from Tilmann et al. (2016), reflecting coupling before the 2010 Maule earthquake. The purple curve denotes 5 m coseismic slip contour lines from An and Meng (2016). CFZ denotes the Challenger Fracture Zone and JFR indicates the Juan-Fernández Ridge. (For interpretation of the references to color in this figure legend, the reader is referred to the web version of this article.)

the five repeater pairs that occurred during the first month following the mainshock (Fig. 4a), but due to the lack of more and precisely located repeater sequences and geodetic constraints, it is uncertain if a slow slip component occurs on the outer-rise faults.

5.2. The early afterslip distribution of the 2015 Illapel event

The afterslip distribution has important implications for the segmentation of the plate interface and how the stress increase induced by the mainshock is released. Fig. 10 shows a comparison of repeating earthquakes and afterslip inverted from geodetic data with the coseismic slip model (An and Meng, 2016) and coupling models inferred from interseismic surface deformation (Métois et al., 2014; Tilmann et al., 2016). We observe a first-order spatial anti-correlation between the afterslip delineated by both repeaters and geodetic inversion and the area of large coseismic slip. This is consistent with observations of the 2011 Tohoku-Oki earthquake (Ozawa et al., 2011), the 2014 Iquique earthquake (Meng et al., 2015) and the 2007 Pisco earthquake along the central Peru megathrust (Perfettini et al., 2010). The large coseismic slip is colocated with an area of strong interseismic coupling. Extensive afterslip may be expected in areas of low interseismic coupling, where static coseismic stress increases can accelerate aseismic slip (e.g., Kato and Igarashi, 2012; Uchida and Matsuzawa, 2013).

To the south of the mainshock rupture area, the observation of afterslip may suggest the changes in pore fluid pressure fields induced by the coseismic rupture or the existence of a relatively weak coupling area. The latter is supported by the coupling model by Tilmann et al. (2016), which shows a transition from strong to weak coupling southward of the Illapel epicenter (Fig. 10b). This supports a scenario in which the mainshock rupture initiates along the edge of the locked patch where the concentration of pre-earthquake loading stress is high. This relatively weakly coupled, velocity strengthening area may have inhibited the southward rupture propagation, which is consistent with the northward unilateral propagation in the initial stage of rupture (e.g., Melgar et al., 2016). To the north of the mainshock rupture, both repeaters and geodetic inversion indicate larger cumulative afterslip in a wider area than the south and downdip. This is consistent with the afterslip distribution obtained by GPS and InSAR inversion in a recent study (Barnhart et al., 2016). This can be well explained by the wide low coupling zone to the north of the rupture zone at ∼30.5°S, which correlates well with the location of the CFZ (Fig. 10, Ruiz et al., 2016). The different afterslip behavior to the north and south of the rupture zone may be explained by the different size and/or mechanical behavior of the low-coupling zones. The low-coupling zones to the north and south of the Illapel rupture area may be explained by the subducting fracture zones or ridges, which can reduce the coupling of the plate interface by inducing fracture networks (Wang and Bilek, 2011; Lange et al., 2016).

Our results suggest that coseismic stress increases lead to rapid afterslip to make up the previously accumulated slip deficit on the along-strike and downdip sections of the mainshock rupture. But it is important to keep in mind that despite the evidence of postseismic slow slip on these zones, future events' dynamic slip may still break through such uncoupled fault sections if rapid shear heating of pore fluids is involved (Noda and Lapusta, 2013). The afterslip moment in the first ∼24 days as inferred from the geodetic measurements is 2.3×10^{20} N m equivalent to Mw = ∼7.51. The cumulative seismic moment release of aftershocks (Mw >= 4) during the corresponding time period amounts to $5.21. \times 10^{19}$ N m (Mw = ∼7.08), indicating that a significant portion (∼77%) of the slip was released by aseismic creep. Note that the calculation of seismic moment excludes the first ∼11-h of aftershocks not spanned by the InSAR data, the total seismic moment released during this period is significant (4.18×10^{20} N m, Mw = ∼7.68). The afterslip expansion in the along-strike direction may lead to enhanced stress loading of the adjacent locked patches of the 1906 M 8.4 earthquake to the south and the 1922 M 8.4 earthquake to the north. This stresses the importance of monitoring of microseismicity and slow slip around these locked zones.

Acknowledgements

We appreciate valuable comments from Diego Melgar and discussions with Zhouchuan Huang. The IRIS (www.iris.edu) data centers provided access to broadband seismograms used in this study. We thank the Centro Sismológico Nacional for providing seismic

and GPS data from their networks. Sentinel-1A interferograms used in our analysis are derived from Copernicus data, subject to ESA use and distribution conditions. This work used computational and storage services associated with the Hoffman2 Shared Cluster provided by UCLA Institute for Digital Research and Education's Research Technology Group. This study is supported by the Knopoff foundation, NSF EAR-1614609 and Special Earthquake Early Warning project 16A43ZX236 of China Earthquake Agency.

Appendix A. Supplementary material

Supplementary material related to this article can be found online at http://dx.doi.org/10.1016/j.epsl.2016.09.055.

References

An, C., Meng, L., 2016. Application of array backprojection to tsunami prediction and early warning. Geophys. Res. Lett. 43. http://dx.doi.org/10.1002/2016GL068786.

Angermann, D., Klotz, J., Reigber, C., 1999. Space-geodetic estimation of the Nazca-South America Euler vector. Earth Planet. Sci. Lett. 171 (3), 329–334.

Barnhart, W.D., Murray, J.R., Briggs, R.W., Gomez, F., Miles, C.P.J., Svarc, J., Riquelme, S., Stressler, B.J., 2016. Coseismic slip and early afterslip of the 2015 Illapel, Chile, earthquake: implications for frictional heterogeneity and coastal uplift. J. Geophys. Res., Solid Earth 121. http://dx.doi.org/10.1002/2016JB013124.

Chen, C.W., Zebker, H.A., 2000. Network approaches to two-dimensional phase unwrapping: intractability and two new algorithms. J. Opt. Soc. Am. 17, 401–414.

Christensen, D.H., Ruff, L.J., 1983. Outer-rise earthquakes and seismic coupling. Geophys. Res. Lett. 10 (8), 697–700.

Dieterich, J., 1994. A constitutive law for rate of earthquake production and its application to earthquake clustering. J. Geophys. Res. 99 (B2), 2601–2618. http://dx.doi.org/10.1029/93JB02581.

Farr, T.G., et al., 2007. The shuttle radar topography mission. Rev. Geophys. 45, RG2004. http://dx.doi.org/10.1029/2005RG000183.

Felzer, K.R., Brodsky, E.E., 2006. Decay of aftershock density with distance indicates triggering by dynamic stress. Nature 441 (7094), 735–738.

Goldstein, R.M., Werner, C.L., 1998. Radar interferogram filtering for geophysical applications. Geophys. Res. Lett. 25, 4035–4038.

Gomberg, J., Bodin, P., Reasenberg, P.A., 2003. Observing earthquakes triggered in the near field by dynamic deformations. Bull. Seismol. Soc. Am. 93 (1), 118–138.

Hayes, G.P., Wald, D.J., Johnson, R.L., 2012. Slab1.0: a three-dimensional model of global subduction zone geometries. J. Geophys. Res. 117, B01302. http://dx.doi.org/ 10.1029/2011JB008524.

Heidarzadeh, M., Murotani, S., Satake, K., Ishibe, T., Gusman, A.R., 2016. Source model of the 16 September 2015 Illapel, Chile, Mw 8.4 earthquake based on teleseismic and tsunami data. Geophys. Res. Lett. 43, 643–650. http://dx.doi.org/10.1002/2015GL067297.

Hill, D.P., Prejean, S.G., 2015. Dynamic triggering. In: Schubert, G. (Ed.), Treatise on Geophysics, 2nd edition. Elsevier, Oxford, pp. 273–304.

Hill, D.P., et al., 1993. Seismicity remotely triggered by the magnitude 7.3 Landers, California, earthquake. Science 260 (5114), 1617–1623.

Hsu, Y.J., Simons, M., Avouac, J.P., Galetzka, J., Sieh, K., Chlieh, M., Natawidjaja, D., Prawirodirdjo, L., Bock, Y., 2006. Frictional afterslip following the 2005 Nias-Simeulue earthquake, Sumatra. Science 312 (5782), 1921–1926.

Igarashi, T., Matsuzawa, T., Hasegawa, A., 2003. Repeating earthquakes and interplate aseismic slip in the northeastern Japan subduction zone. J. Geophys. Res. 108, 2249.

Kato, A., Igarashi, T., 2012. Regional extent of the large coseismic slip zone of the 2011 Mw 9.0 Tohoku-Oki earthquake delineated by on-fault aftershocks. Geophys. Res. Lett. 39, L15301. http://dx.doi.org/10.1029/2012GL052220.

Kato, A., Obara, K., 2014. Step-like migration of early aftershocks following the 2007 Mw 6.7 Noto-Hanto earthquake, Japan. Geophys. Res. Lett. 41, 3864–3869. http://dx.doi.org/10.1002/2014GL060427.

Kato, A., Obara, K., Igarashi, T., Tsuruoka, H., Nakagawa, S., Hirata, N., 2012. Propagation of slow slip leading up to the 2011 Mw 9.0 Tohoku-Oki earthquake. Science 335, 705–708.

Kilb, D., Gomberg, J., Bodin, P., 2000. Triggering of earthquake aftershocks by dynamic stresses. Nature 408 (6812), 570–574.

Lange, D., Geersen, J., Barrientos, S., Moreno, M., Grevemeyer, I., Contreras-Reyes, E., Kopp, H., 2016. Aftershock seismicity and tectonic setting of the 16 September 2015 Mw 8.3 Illapel earthquake, Central Chile. Geophys. J. Int. 206, 1424–1430, ggw218.

Laursen, J., Normark, W.R., 2002. Late Quaternary evolution of the San Antonio Submarine Canyon in the central Chile forearc (∼33S). Mar. Geol. 188 (3), 365–390.

Lay, T., Kanamori, H., Ammon, C.J., Hutko, A.R., Furlong, K., Rivera, L., 2009. The 2006–2007 Kuril Islands great earthquake sequence. J. Geophys. Res. 114, B11308. http://dx.doi.org/10.1029/2008JB006280.

Lengliné, O., Enescu, B., Peng, Z., Shiomi, K., 2012. Decay and expansion of the early aftershock activity following the 2011, Mw 9.0 Tohoku earthquake. Geophys. Res. Lett. 39, L18309. http://dx.doi.org/10.1029/2012GL052797.

Marone, C., 1998. Laboratory-derived friction laws and their application to seismic faulting. Annu. Rev. Earth Planet. Sci. 26, 643–696.

Melgar, D., Fan, W., Riquelme, S., Geng, J., Liang, C., Fuentes, M., Vargas, G., Allen, R.M., Shearer, P.M., Fielding, E.J., 2016. Slip segmentation and slow rupture to the trench during the 2015, Mw8.3 Illapel, Chile earthquake. Geophys. Res. Lett. 43, 961–966. http://dx.doi.org/10.1002/2015GL067369.

Meng, L., Huang, H., Bürgmann, R., Ampuero, J.P., Strader, A., 2015. Dual megathrust slip behaviors of the 2014 Iquique earthquake sequence. Earth Planet. Sci. Lett. 411, 177–187.

Métois, M., Socquet, A., Vigny, C., 2012. Interseismic coupling, segmentation and mechanical behavior of the central Chile subduction zone. J. Geophys. Res. 117, B03406. http://dx.doi.org/10.1029/2011JB008736.

Métois, M., Vigny, C., Socquet, A., Delorme, A., Morvan, S., Ortega, I., Valderas-Bermejo, C.-M., 2014. GPS-derived interseismic coupling on the subduction and seismic hazards in the Atacama region, Chile. Geophys. J. Int. 196 (2), 644–655. http://dx.doi.org/10.1093/gji/ggt418.

Nadeau, R.M., Johnson, L.R., 1998. Seismological studies at Parkfield VI: moment release rates and estimates of source parameters for small repeating earthquakes. Bull. Seismol. Soc. Am. 88, 790–814.

Nadeau, R.M., McEvilly, T.V., 1999. Fault slip rates at depth from recurrence intervals of repeating microearthquakes. Science 285, 718–721.

Nikkhoo, M., Walter, T.R., 2015. Triangular dislocation: an analytical, artefact-free solution. Geophys. J. Int. 2, 1117–1139. http://dx.doi.org/10.1093/gji/ggv035.

Noda, H., Lapusta, N., 2013. Stable creeping fault segments can become destructive as a result of dynamic weakening. Nature 493 (7433), 518–521.

Okuwaki, R., Yagi, Y., Aránguiz, R., González, J., González, G., 2016. Rupture process during the 2015 Illapel, Chile earthquake: zigzag-along-dip rupture episodes. Pure Appl. Geophys. 173, 1011–1020. http://dx.doi.org/10.1007/s00024-016-1271-6.

Ozawa, S., Nishimura, T., Suito, H., Kobayashi, T., Tobito, M., Imakiire, T., 2011. Coseismic and postseismic slip of the 2011 magnitude-9 Tohoku-Oki earthquake. Nature 475, 373–376. http://dx.doi.org/10.1038/nature10227.

Peng, Z., Zhao, P., 2009. Migration of early aftershocks following the 2004 Parkfield earthquake. Nat. Geosci. 2, 877–881.

Perfettini, H., Avouac, J.-P., 2004. Postseismic relaxation driven by brittle creep: a possible mechanism to reconcile geodetic measurements and the decay rate of aftershocks, application to the Chi-Chi earthquake, Taiwan. J. Geophys. Res. 109, B02304. http://dx.doi.org/10.1029/2003JB002488.

Perfettini, H., Avouac, J.P., Tavera, H., Kositsky, A., Nocquet, J.M., Bondoux, F., Soler, P., 2010. Seismic and aseismic slip on the Central Peru megathrust. Nature 465 (7294), 78–81.

Ruiz, S., Klein, E., del Campo, F., Rivera, E., Poli, P., Métois, M., Vigny, C., Baez, J.C., Vargas, G., Leyton, F., Madariaga, R., Fleitout, L., 2016. The seismic sequence of the 16 September 2015 Mw 8.3 Illapel, Chile, earthquake. Seismol. Res. Lett. 87. http://dx.doi.org/10.1785/0220150281.

Salvi, S., Stramondo, S., Funning, G.J., Ferretti, A., Sarti, F., Mouratidis, A., 2012. The Sentinel-1 mission for the improvement of the scientific understanding and the operational monitoring of the seismic cycle. Remote Sens. Environ. 120, 164–174. http://dx.doi.org/10.1016/j.rse.2011.09.029.

Shirzaei, M., Bürgmann, R., Taira, T., 2013. Implications of recent asperity failures and aseismic creep for time-dependent earthquake hazard on the Hayward fault. Earth Planet. Sci. Lett. 371–372, 59–66. http://dx.doi.org/10.1016/j.epsl.2013.04.024.

Templeton, D.C., Nadeau, R.M., Bürgmann, R., 2008. Behavior of repeating earthquake sequences in Central California and the implications for subsurface fault creep. Bull. Seismol. Soc. Am. 98, 52–65.

Tilmann, F., et al., 2016. The 2015 Illapel earthquake, central Chile: a type case for a characteristic earthquake? Geophys. Res. Lett. 43, 574–583. http://dx.doi.org/10.1002/2015GL066963.

Uchida, N., Matsuzawa, T., 2013. Pre- and postseismic slow slip surrounding the 2011 Tohoku-oki earthquake rupture. Earth Planet. Sci. Lett. 374, 81–91.

Uchida, N., Hasegawa, A., Matsuzawa, T., Igarashi, T., 2004. Pre- and postseismic slow slip on the plate boundary off Sanriku, NE Japan associated with three interplate earthquakes as estimated from small repeating earthquake data. Tectonophysics 385, 1–15.

van der Elst, N.J., Brodsky, E.E., 2010. Connecting near-field and far-field earthquake triggering to dynamic strain. J. Geophys. Res. 115 (B07311). http://dx.doi.org/10.1029/2009JB006681.

Wang, K., Bilek, S.L., 2011. Do subducting seamounts generate or stop large earthquakes? Geology 39, 819–822.

Yáñez, G.A., Ranero, C.R., vonHuene, R., Díaz, J., 2001. Magnetic anomaly interpretation across the southern central Andes (32°–34°S): the role of the Juan Fernández Ridge in the late Tertiary evolution of the margin. J. Geophys. Res. 106 (B4), 6325–6345. http://dx.doi.org/10.1029/2000JB900337.

Yin, J., Yang, H., Yao, H., Weng, H., 2016. Coseismic radiation and stress drop during the 2015 Mw 8.3 Illapel, Chile megathrust earthquake. Geophys. Res. Lett. 43, 1520–1528. http://dx.doi.org/10.1002/2015GL067381.

Zhang, M., Wen, L., 2015. An effective method for small event detection: Match and locate (M&L). Geophys. J. Int. 200 (3), 1523–1537.